Appendix

A. More on Experimental Results

In this part, we give additional results and details of our models.

A.1. MedMNIST datasets.

While the main part of our paper focuses on the Breast Ultrasound setting to maintain a clear scope, we also demonstrate the versatility and adaptability of our topological vectors and their significant contributions to existing deep learning models by showcasing their performance across various medical image formats. Utilizing the MedMNIST dataset [78], we employed three benchmark datasets, RETI-NAMNIST, PneuMNIST and BloodMNIST(see Table 8), applying our Betti-CNN model to 128 × 128 images with predefined splits. Note that the BreastMNIST dataset corresponds to the BUSI dataset used in this paper. The performance of our model for BUSI is detailed in the main text (see Table 2).

Table 8. MedMNIST Dataset Details. * means varying image sizes.

MedMNIST2D	Data Modality	Image size	# Classes	# Samples	Train/Valid/Test
PneuMNIST	Chest X-ray	$1650\times1420^*$	2	5,856	4,708 / 524 / 624
RetinaMNIST	Fundus Camera	1736×1824	5	1,600	1,080 / 120 / 400
BreastMNIST	Breast Ultrasound	500×500	2	780	546 / 78 / 156
BloodMNIST	Blood Cell Microscope	200×200	8	17,092	11,959 / 1,712 / 3,421

Table 9. ML Classifiers. Performance of our basic Topo-ML model with XGBoost, MLP and Transformer classifiers on breast ultrasound datasets.

		A	Accurac	y	AUC				
Dataset	Class	XGB	MLP	TF	XGB	MLP	TF		
BUSI	2	77.78	82.81	68.01	81.81	85.33	67.94		
BUSI	3	70.01	66.28	60.38	83.12	78.29	73.86		
MENDELEY	2	94.00	96.00	77.20	97.13	97.67	83.72		
BUS-BRA	2	68.42	63.10	88.48	66.28	57.80	95.14		

A.2. Comparison with Other Topo-DL Models

We conducted experiments using PHG-Net [50], and the performance comparison in terms of AUC and Accuracy is presented in Table 10.

Table 10. Comparison of Topo-DL Models. AUC and Accuracy comparisons for PHG-Net and Topo-Swin.

	Accu	racy	AUC				
Dataset	PHG-NET	Topo-VT	PHG-NET	Topo-VT			
BUSI-2	86.6	86.9	94.7	95.9			
BUSI-3	87.4	91.0	96.7	97.5			
BUS-BRA	83.0	95.7	90.1	99.5			
MENDELEY	99.6	99.2	99.6	99.9			

A.3. Additional Performance Metrics

In medical image analysis, F1-scores is a very common metric incorporating both precision and recall. Precision (also called positive predictive value) measures the accuracy of positive predictions, while recall (also called sensitivity or true positive rate) measures the proportion of actual positives that were correctly identified by the model. The F1-score is the harmonic mean of precision and recall and

is calculated as
$$F_1 = 2 \times \frac{\text{precision} \times \text{recall}}{\text{precision} + \text{recall}}$$
.

In Table 11, we present the F1-scores of our models. It's worth noting that although the improvements may appear marginal, our findings in Table 13 demonstrate that most of these enhancements are statistically highly significant.

Table 11. Comparison of F1-scores between CNN and Topo-CNN models.

	MENDELEY			BUS-BRA			BUSI 2-Labels			BUSI 3-Labels		
MODEL	CNN	B-CNN	P-CNN	CNN	B-CNN	P-CNN	CNN	B-CNN	P-CNN	CNN	B-CNN	P-CNN
DenseNet121	97.72	98.33	99.81	74.65	77.37	76.32	84.32	87.09	88.31	81.29	83.47	84.63
EfficientNetB0	96.79	97.51	97.60	76.88	79.87	78.20	85.86	88.41	87.59	82.69	84.42	84.49
IncResNetV2	93.18	97.86	99.42	75.25	74.35	75.16	74.35	87.59	87.73	80.25	82.77	83.64
InceptionV3	98.79	98.66	100.0	73.62	73.30	73.07	84.08	85.85	86.22	79.77	82.30	81.16
MobileNetV2	98.66	98.35	99.63	75.25	76.78	76.51	85.35	86.94	87.28	82.65	84.01	80.56
ResNet50	99.77	99.24	99.62	77.80	80.04	78.94	86.97	88.58	88.20	83.87	85.18	85.33
ResNet101	99.73	99.36	98.91	78.62	80.03	79.91	88.42	89.86	88.98	84.96	85.98	86.02
VGG16	98.55	99.27	99.23	72.30	76.35	74.68	86.37	89.28	89.86	81.63	84.86	84.57

Table 12. Performance metrics for SwinV2 and Topo-VT models.

			SwinV	2		Topo-VT						
Dataset	Acc	AUC	Prec	Recall	F1	Acc	AUC	Prec	Recall	F1		
BUSI-2	91.34	96.01	91.29	89.14	89.84	86.89	95.87	89.79	81.00	83.10		
BUSI-3	90.26	97.35	90.84	88.11	89.01	91.03	97.45	90.05	90.62	90.13		
BUS-BRA	85.65	92.98	84.38	83.68	83.42	95.74	99.54	94.83	95.57	95.19		
MENDELEY	98.80	100.0	99.09	98.50	98.71	99.20	99.97	99.38	99.00	99.15		

A.4. Significance Test.

In Table 2 and Table 11, we outlined the three performance metrics for vanilla-CNN and our Topo-CNN models, highlighting the integration of topological features into conventional CNN architectures has potential to enhance the breast cancer screening. To evaluate the statistical significance of these enhancements, we utilized two distinct methods: the t-test and the Wilcoxon signed-rank test. The results, including all p-values, are documented in Table 13 and Table 14. A significant majority of these p-values fell below the 0.05 threshold, indicating statistical significance, and are accordingly highlighted in blue for easy identification

Our analysis showed that the B-CNN model outperformed the standard CNN model with a notable margin, as evidenced by the prevalence of blue in its respective subsection. Similarly, the P-CNN model demonstrated a significant improvement over the conventional CNN, with more

Table 13. Summary of p-values derived from t-tests indicating the performance disparity between vanilla-CNN and Topo-CNN models (Betti-CNN and Persistence Image-CNN) through t-test for BUSI, BUS-BRA, and MENDELEY datasets. To condense, we denote e^n as 10^n . Outcomes with p < 0.05 are statistically significant and are highlighted in blue.

			I	BUSI 2-la	bel				
	$ \begin{array}{c ccccccccccccccccccccccccccccccccccc$			CN	N vs P-C	NN	P-CNN vs B-CNN		
MODEL	ACC	AUC	F-1	ACC	AUC	F-1	ACC	AUC	F-1
DenseNet121									
EfficientNetB0									
InceptionV3	$1.5e^{-06}$	$1.1e^{-08}$	$1.3e^{-05}$	$4.5e^{-02}$	$1.5e^{-01}$	$7.2e^{-02}$	$6.4e^{-01}$	$1.1e^{-01}$	$6.0e^{-01}$
IncResNetV2									
MobileNetV2									
ResNet101									
ResNet50									
VGG16	$9.4e^{-12}$	$5.5e^{-11}$	$7.3e^{-11}$	$1.2e^{-06}$	$2.8e^{-02}$	$3.1e^{-04}$	$9.1e^{-01}$	$2.9e^{-01}$	$7.5e^{-01}$

			I	BUSI 3-la	bel				
	CN	N vs B-C	NN	CN	N vs P-C	NN	P-CNN vs B-CNN		
MODEL	ACC	AUC	F-1	ACC	AUC	F-1	ACC	AUC	F-1
DenseNet121				$1.2e^{-10}$					
EfficientNetB0									
InceptionV3				$1.3e^{-02}$					
IncResNetV2				$2.1e^{-07}$					
MobileNetV2				$1.0e^{-00}$					
ResNet101				$6.0e^{-03}$					
ResNet50				$1.0e^{-03}$					
VGG16	$6.6e^{-08}$	$2.8e^{-07}$	$1.1e^{-08}$	$5.9e^{-08}$	$7.1e^{-01}$	$4.0e^{-09}$	$2.7e^{-01}$	$1.5e^{-07}$	$2.5e^{-01}$

				BUS-BR	A				
	CN	N vs B-C	NN	CN	N vs P-C	NN	P-CNN vs B-CNN		
MODEL	ACC	AUC	F-1	ACC	AUC	F-1	ACC	AUC	F-1
								$5.0e^{-05}$	
EfficientNetB0									
InceptionV3								$1.3e^{-06}$	
IncResNetV2								$3.5e^{-02}$	
MobileNetV2								$1.8e^{-06}$	
ResNet101								$1.1e^{-03}$	
ResNet50								$2.3e^{-04}$	
VGG16	$2.3e^{-17}$	$2.9e^{-11}$	$2.2e^{-13}$	$5.3e^{-11}$	$1.0e^{-00}$	$6.3e^{-06}$	$5.1e^{-02}$	$2.0e^{-09}$	$3.8e^{-04}$

	MENDELEY										
	CN	N vs B-C	NN	CN	CNN vs P-CNN			P-CNN vs B-CNN			
MODEL	ACC	AUC	F-1	ACC	AUC	F-1	ACC	AUC	F-1		
DenseNet121	$1.3e^{-03}$	$3.3e^{-02}$	$8.0e^{-04}$	$4.7e^{-09}$	$5.3e^{-07}$	$7.4e^{-09}$	$1.0e^{-00}$	$1.0e^{-00}$	$1.0e^{-00}$		
EfficientNetB0					$5.0e^{-06}$						
InceptionV3					$8.9e^{-05}$						
IncResNetV2					$7.7e^{-14}$						
MobileNetV2					$1.5e^{-06}$						
ResNet101					$7.3e^{-01}$						
ResNet50					$4.3e^{-02}$						
VGG16	$3.9e^{-07}$	$1.9e^{-03}$	$1.0e^{-05}$	$3.4e^{-03}$	$4.4e^{-06}$	$4.5e^{-02}$	$5.7e^{-01}$	$1.0e^{-00}$	$4.5e^{-01}$		

than half of the comparative tests yielding significant results, also marked in blue. When comparing P-CNN against B-CNN, our findings suggest a superior performance by B-CNN, particularly on the BUSI and BUS-BRA datasets.

To conclude, the statistical evidence supports that both Topo-CNN models, namely P-CNN and B-CNN, significantly surpass the baseline CNN model in terms of performance by leveraging topological features. Despite this, the performance gap between P-CNN and B-CNN, while present, often does not reach statistical significance, suggesting a nuanced comparison that varies by dataset and context.

A.5. Persistence Images and PI-CNN model

To explore the effect of vectorization on our models, we also employed a different vectorization to replace Betti vectors in our models.

Table 14. Summary of p-values derived from Wilcoxon signed-rank test indicating the performance disparity between vanilla-CNN and Topo-CNN models (Betti-CNN and Persistence Image-CNN) through t-test for BUSI, BUS-BRA, and MENDELEY datasets. To condense, we denote e^n as 10^n . Outcomes with p < 0.05 are statistically significant and are highlighted in blue.

			I	BUSI 2-la	bel				
	CN	N vs B-C	NN	CN	N vs P-C	NN	P-CNN vs B-CNN		
MODEL	ACC	AUC	F-1	ACC	AUC	F-1	ACC	AUC	F-1
				$1.0e^{-04}$					
EfficientNetB0									
InceptionV3				$8.6e^{-03}$					
IncResNetV2				$9.5e^{-07}$					
MobileNetV2				$3.3e^{-03}$					
ResNet101				$8.2e^{-02}$					
ResNet50				$5.3e^{-03}$					
VGG16	$9.5e^{-07}$	$9.5e^{-07}$	$9.5e^{-07}$	$9.5e^{-07}$	$6.6e^{-02}$	$5.1e^{-04}$	$9.2e^{-01}$	$3.6e^{-01}$	$7.1e^{-01}$

			I	BUSI 3-la	bel				
	CN	N vs B-C	NN	CN	N vs P-C	NN	P-CNN vs B-CNN		
MODEL	ACC	AUC	F-1	ACC	AUC	F-1	ACC	AUC	F-1
				$4.8e^{-05}$					
EfficientNetB0									
InceptionV3				$1.3e^{-02}$					
IncResNetV2				$6.5e^{-05}$					
MobileNetV2	$3.6e^{-03}$	$3.2e^{-01}$	$1.6e^{-04}$	$1.0e^{-00}$	$1.0e^{-00}$	$1.0e^{-00}$	$3.1e^{-05}$	$9.5e^{-07}$	$1.3e^{-05}$
ResNet101				$8.8e^{-03}$					
ResNet50				$1.6e^{-03}$					
VGG16	$4.8e^{-06}$	$1.9e^{-06}$	$2.9e^{-06}$	$7.5e^{-05}$	$5.8e^{-01}$	$2.9e^{-06}$	$2.0e^{-01}$	$9.5e^{-07}$	$2.0e^{-01}$

				BUS-BR	A					
	CN	CNN vs B-CNN			CNN vs P-CNN			P-CNN vs B-CNN		
MODEL	ACC	AUC	F-1	ACC	AUC	F-1	ACC	AUC	F-1	
				$ 6.8e^{-03} $						
EfficientNetB0										
InceptionV3				$1.5e^{-01}$						
IncResNetV2	$6.8e^{-01}$	$1.0e^{-00}$	$8.8e^{-01}$	$1.8e^{-02}$	$1.0e^{-00}$	$7.8e^{-01}$	$9.7e^{-01}$	$1.8e^{-02}$	$8.1e^{-01}$	
MobileNetV2				$2.9e^{-06}$						
ResNet101				$3.6e^{-04}$						
ResNet50				$1.6e^{-02}$						
VGG16	$4.8e^{-05}$	$9.5e^{-07}$	$9.5e^{-07}$	$4.8e^{-05}$	$1.0e^{-00}$	$2.9e^{-06}$	$7.0e^{-03}$	$1.9e^{-06}$	$4.3e^{-04}$	

MENDELEY									
	CNN vs B-CNN			CNN vs P-CNN			P-CNN vs B-CNN		
MODEL	ACC	AUC	F-1	ACC	AUC	F-1	ACC	AUC	F-1
				$ 5.1e^{-05} $					
EfficientNetB0									
InceptionV3				$4.5e^{-05}$					
IncResNetV2				$4.7e^{-05}$					
MobileNetV2				$7.5e^{-04}$					
ResNet101				$3.3e^{-01}$					
ResNet50				$7.7e^{-02}$					
VGG16	$1.1e^{-04}$	$6.9e^{-04}$	$4.1e^{-05}$	$1.3e^{-02}$	$4.7e^{-05}$	$1.2e^{-01}$	$8.8e^{-01}$	$1.0e^{-00}$	$8.8e^{-01}$

Persistence Images. Persistence Images is one of the most common vectorization methods in TDA, introduced by Adams et al. [2]. Unlike most vectorizations, Persistence Images, as the name suggests, produce 2D-arrays (tensors). The idea is to capture the location of the points in the PDs with a multivariable function by using the 2D Gaussian functions centered at these points. For $PD(\mathbf{G}) = \{(b_i,d_i)\}$, let ϕ_i represent a 2D-Gaussian centered at the point $(b_i,d_i) \in \mathbb{R}^2$. Then, one defines a multivariable function, $Persistence\ Surface,\ \widetilde{\mu} = \sum_i w_i \phi_i$ where w_i is the weight, mostly a function of the life span $d_i - b_i$. To represent this multivariable function as a 2D-vector, one defines a $k \times l$ grid (resolution size) on the domain of $\widetilde{\mu}$, i.e., threshold domain of $PD(\mathbf{G})$. Then, one obtains the $Persistence\ Image$, a 2D-vector (matrix) $\overrightarrow{\mu} = [\mu_{rs}]$ of size $k \times l$ such that

$$\mu_{rs} = \int_{\Delta_{rs}} \widetilde{\mu}(x, y) \, dx dy$$

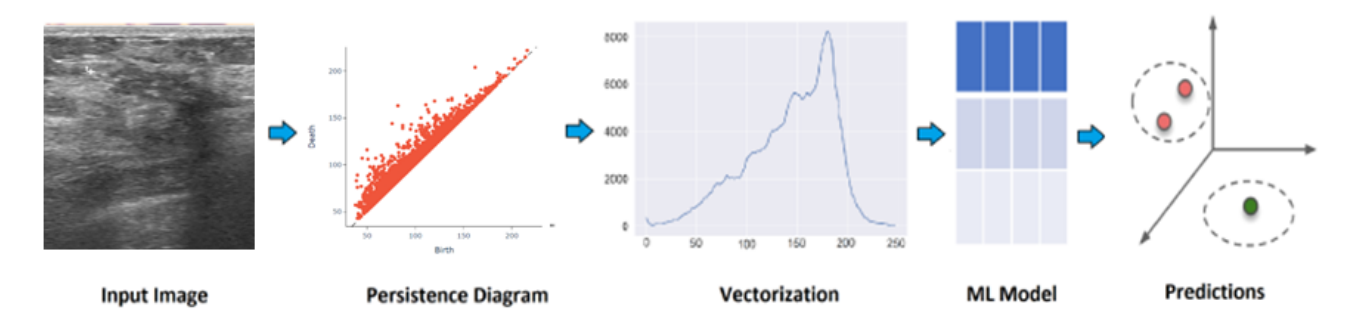


Figure 9. Topo-ML model. In our basic model, we first generate persistence diagrams for any input image. Next, we derive our topological feature vectors, which are then inputted into an ML classifier to produce classification results.

where $\Delta_{rs} = \text{ pixel with index } rs \text{ in the } k \times l \text{ grid.}$

Note that the resolution size $k \times l$ is independent of the number of thresholds used in the filtering; the choice of k and l is completely up to the user. There are two other important tuning parameters for persistence images, namely the weight w_i and the variance σ (the width of the Gaussian functions). Like Silhouettes, one can choose $w_i = (d_i - b_i)^p$ to emphasize large or small features in the PD. Similarly, the width parameter σ determines the sharpness of Gaussian, where smaller σ would make the Gaussian functions more like Dirac δ -function, and larger σ would make the Gaussians flat. Depending on the context, σ can be chosen a constant (e.g. $\sigma = 0.1$) or depending on the point (b_i, d_i) , e.g., $\sigma_i = k(d_i - b_i)$ for some constant k > 0.

Hyperparameters for PI-CNN model. For each image \mathcal{X} , we first generated two 50 by 50 persistence images $\mathcal{PI}_0(\mathcal{X})$ and $\mathcal{PI}_1(\mathcal{X})$ corresponding to homology groups 0 and 1 respectively. These two persistence images were concatenated to obtain 50 by 100 matrix, which serves as a topological representation for each 2D image.

Our PI-CNN model (Figure Figure 3) integrates a pretrained CNN with inputs of size 224×224 with additional frozen layers, enhanced by a 2D Multi-Layer Perceptron (2D MLP). The augmented CNN includes a convolutional layer with 64 filters of size (3, 3) and ReLU activation, followed by a max-pooling layer with a pool size of (2, 2), a flatten layer, and a dense layer with 64 neurons. Simultaneously, the 2D MLP consists of a convolutional layer with 32 filters of size (3, 3), a max pooling layer of size (2, 2), a flatten layer, and a dense layer with 128 neurons using ReLU activation. The concatenated outputs from both models are further processed by fully connected layers, including 256, 128, and 128 neurons each with ReLU activation, culminating in the model's final output.

B. Alexander Duality for Cubical Persistence

In this section, we show the duality between sublevel filtration and superlevel filtration for cubical persistence. We note that in [9], the authors prove a duality result for cu-

bical complexes, however their duality results are completely unrelated to ours. In their work, the authors study pixel connectivity in cubical complexes and construct *dual graph filtrations* for given cubical complex filtration. In our case, we relate one cubical complex filtration to another one (sublevel-superlevel) and show their duality in complementary dimensions.

First, we recall some earlier results from algebraic topology, which is essential for the proof. Next, we give the setup and introduce the notation which we use in upcoming sections.

B.1. Preliminaries

In this part, we recall some of the well-known results which we use in the proof of the duality theorem [33].

Lemma 2 (Alexander Duality) *Let* \mathcal{X} *be a compact, locally contractible subspace of d-sphere* \mathbf{S}^d . *Then,*

$$\widetilde{H}_k(\mathcal{X}) \simeq \widetilde{H}^{d-k-1}(\mathbf{S}^d - \mathcal{X})$$

where \widetilde{H} represents reduced (co)homology.

Since we only use field coefficients **F** in persistence modules, the Universal Coefficients Theorem [33] comes in a very simple form as follows.

Lemma 3 (Universal Coefficients Theorem) *Let* \mathbf{F} *be a field. Then, for any* k*,*

$$H^k(\mathcal{X}; \mathbf{F}) \simeq \operatorname{Hom}(H_k(\mathcal{X}; \mathbf{F}), \mathbf{F}) \simeq H_k(\mathcal{X}; \mathbf{F})$$

Next, we will need the following duality result between persistent homology and persistent cohomology [21].

Lemma 4 (Persistent Cohomology) For a given filtration $\{\mathcal{X}_n\}$, persistent homology $(H_k(\mathcal{X}_i) \to H_k(\mathcal{X}_j))$ and persistent cohomology $(H^k(\mathcal{X}_i) \leftarrow H^k(\mathcal{X}_j))$ have identical barcodes:

$$PD({H_k(\mathcal{X}_i)}) \simeq PD({H^k(\mathcal{X}_i)})$$

Finally, we quote the celebrated result on the uniqueness of the barcode decomposition in persistence module [10].

Lemma 5 (Krull-Schmidt Theorem) Any finite-dimensional persistence module has a unique (up to isomorphism) decomposition into indecomposable modules.

In other words, the dimension of the homology groups $\{H_k(\mathcal{X}_i)\}$, and ranks of the homomorphisms $\varphi_{ij}: H_k(\mathcal{X}_i) \to H_k(\mathcal{X}_j)$, uniquely determines the persistence barcode. Here, each bar in the persistence barcode corresponds to an indecomposable module in the theorem.

B.2. Notation and Setup

In the following, we will work with 3 different cubical complexes (CC): The original CC \mathcal{X} , the extended CC $\widehat{\mathcal{X}}$, and the extended sphere $\widehat{\mathcal{X}}$.

The image \mathcal{X} : Let \mathcal{X} be a d-dimensional cubical complex of resolution $\mathcal{R}=r_1\times r_2\times \cdots \times r_d=\Pi_{j=1}^d r_j$. Let $\eta=(\eta_1,\eta_2,\ldots,\eta_N)$ represent the index of the voxels in the cubical complex \mathcal{X} , i.e., $1\leq \eta_j\leq r_j$. By abusing the notation, we will call the collection of voxels in \mathcal{X} as $\mathcal{R}=\{\Delta_\eta\}$. Let $f:\mathcal{R}\to\mathbb{R}$ be the filtering function assigning each voxel Δ_η with corresponding (color) value $f(\eta)$. Let $m=\min f$ and $M=\max f$. Notice that the only interesting persistence diagrams for d-dimensional cubical complex are $k=0,1,2,\ldots,d-1$ as for $k\geq d$, $\mathrm{PD}_k(\mathcal{X})$ is trivial.

The extended (padded) image $\widehat{\mathcal{X}}$: First, we induce a slightly larger complex $\widehat{\mathcal{X}}$ of resolution $\widehat{\mathcal{R}} = \prod_{j=1}^N (r_j + 2)$ with indices $\eta = (\eta_1, \eta_2, \dots, \eta_N)$ again where $0 \leq \eta_j \leq r_j + 1$. In other words, we attach a padding of thickness-1 along the boundary of our original cubical complex \mathcal{X} . Then, we extend f to \widehat{f} such that $\widehat{f}(\eta) = f(\eta)$ for any $\eta \in \mathcal{R}$, and $\widehat{f}(\eta) = M$ for any $\eta \in \widehat{\mathcal{R}} - \mathcal{R}$, e.g., the value of $\widehat{f} = M$ for any voxel in the boundary shell $\widehat{\mathcal{X}} - \mathcal{X}$.

The extended sphere $\widetilde{\mathcal{X}}$: Our second extension is to double $\widehat{\mathcal{X}}$ topologically and obtain a d-sphere $\widetilde{\mathcal{X}}$. In particular, glueing two d-balls along their boundaries with an identity map gives a d-sphere [33]. Here, we do the same by taking an exact copy of $\widehat{\mathcal{X}}$ and glue it to the original one along the boundary. Hence, we double the number of voxels in $\widehat{\mathcal{X}}$, and we have a new index set $\widehat{\mathcal{R}} = 2 \cdot \widehat{\mathcal{R}}$. Again, we extend f to $\widetilde{\mathcal{X}}$ as before. i.e., $\widetilde{f}(\eta) = f(\eta)$ for any $\eta \in \mathcal{R}$, and $\widetilde{f}(\eta) = M$ for any $\eta \in \widehat{\mathcal{R}} - \mathcal{R}$. In other words, in the d-sphere \widetilde{X} , \widetilde{f} is defined as M for any voxel in $\widetilde{\mathcal{X}} - \mathcal{X}$.

In the following, we will represent k^{th} persistence diagram for sublevel filtration as $\mathrm{PD}_k^{\uparrow}(\mathcal{X},f)$ and k^{th} persistence diagram for superlevel filtration as $\mathrm{PD}_k^{\downarrow}(\mathcal{X},f)$.

B.3. Proof of the Theorem

Now, we are ready to prove our main duality result. In the following theorem, we prove the equivalence of persistence diagrams of sublevel and superlevel filtrations in complementary dimensions. In Remark 7, we give the explicit description of the correspondence between the bars in these persistence barcodes.

Theorem 6 Let \mathcal{X} be a cubical complex of dimension d, and f be the filtering function on \mathcal{X} . Let $\widehat{\mathcal{X}}$ be its extended image with \widehat{f} . Then, the persistence diagrams for the sublevel and superlevel filtration of $\widehat{\mathcal{X}}$ with respect to \widehat{f} in complementary dimensions are equivalent.

$$\mathrm{PD}_k^\uparrow(\widehat{X},\widehat{f}) \simeq \mathrm{PD}_{d-k-1}^\downarrow(\widehat{\mathcal{X}},\widehat{f})$$

Proof: We prove the theorem in 2 steps. In the first step, we prove the duality in the sphere setting $(\widetilde{\mathcal{X}})$. In this version, we prove the equivalence between the *reduced* persistence diagrams which means that for dimension k=0, the main barcode corresponding to the connected component with infinite lifespan is removed. Then, in the second step, we adapt this result to *extended* images $(\widehat{\mathcal{X}})$ setting and finish the proof.

Step 1: Let $\widetilde{\mathcal{X}}$ be the extended sphere of \mathcal{X} , and \widetilde{f} be the corresponding extension of f. Then, the following *reduced* persistence diagrams are equivalent:

$$\mathrm{PD}_{k}^{\uparrow}(\widetilde{X},\widetilde{f}) \simeq \mathrm{PD}_{d-k-1}^{\downarrow}(\widetilde{\mathcal{X}},\widetilde{f})$$

Proof of Step 1: Let $t_0 < t_1 = \min f < t_2 < \cdots < t_{N-1} < t_N = \max f$ be the threshold set for f. Let $\widetilde{\mathcal{R}}_n = \{\eta \in \widetilde{\mathcal{R}} \mid \widetilde{f}(\eta) \leq t_n\}$. As before, define the sublevel filtration for $\widetilde{\mathcal{X}}$ such that $\widetilde{\mathcal{X}}_n = \bigcup_{\eta \in \widetilde{\mathcal{R}}_n} \Delta_{\eta}$. i.e., $\emptyset = \widetilde{\mathcal{X}}_0 \subset \widetilde{\mathcal{X}}_1 \subset \cdots \subset \widetilde{\mathcal{X}}_{N-1} \subset \widetilde{\mathcal{X}}_N = \widetilde{\mathcal{X}}$. Similarly, let $\widetilde{\mathcal{R}}^n = \widetilde{\mathcal{R}} - \widetilde{\mathcal{R}}_n = \{\eta \in \widetilde{\mathcal{R}} \mid \widetilde{f}(\eta) > t_n\}$. Now, the superlevel filtration can be defined as $\widetilde{\mathcal{X}}^n = \bigcup_{\eta \in \mathcal{R}^n} \Delta_{\eta}$, i.e., $\emptyset = \widetilde{\mathcal{X}}^N \subset \widetilde{\mathcal{X}}^{N-1} \subset \cdots \subset \widetilde{\mathcal{X}}^2 \subset \widetilde{\mathcal{X}}^1 \subset \widetilde{\mathcal{X}}^0 = \widetilde{\mathcal{X}}$. Note that to avoid crowding the notation, we slightly modify superlevel filtration with strict inequality $(\widetilde{f}(\eta) > t_n)$. This only shifts the indexes by one from the original superlevel filtration $(\widetilde{f}(\eta) \geq t_n)$ (Section 3.1).

By definition, we have $\widetilde{\mathcal{X}} - \widetilde{\mathcal{X}}_n = \widetilde{\mathcal{X}}^n$. Recall that \widetilde{X} is a d-sphere. Hence, by Alexander duality (Lemma 2), for any 0 < k < d-1, we have

$$\widetilde{H}_k(\widetilde{\mathcal{X}}_n) \simeq \widetilde{H}^{d-k-1}(\widetilde{\mathcal{X}}^n)$$
 (1)

Notice that the Alexander duality uses reduced homology, hence infinite barcode for k=0 is removed in this correspondence. Now, consider the persistent cohomology induced by the filtration $\{\widetilde{\mathcal{X}}^n\}$, where $H^k(\widetilde{\mathcal{X}}^i) \to H^k(\widetilde{\mathcal{X}}^j)$ as $\widetilde{\mathcal{X}}^i \supset \widetilde{\mathcal{X}}^j$ for i < j. Notice that by the naturality of

 $H^k(\mathcal{X}; \mathbf{F}) = \text{Hom}(H_k(\mathcal{X}; \mathbf{F}), \mathbf{F})$ (Lemma 3), we have the following commutative diagram:

$$\widetilde{H}_{k}(\widetilde{\mathcal{X}}_{i}) \xrightarrow{\varphi} \widetilde{H}_{k}(\widetilde{\mathcal{X}}_{j})
\downarrow \simeq \qquad \qquad \downarrow \simeq \qquad (2)
\widetilde{H}^{d-k-1}(\widetilde{\mathcal{X}}^{i}) \xrightarrow{\varphi^{*}} \widetilde{H}^{d-k-1}(\widetilde{\mathcal{X}}^{j})$$

Now, we claim that k^{th} persistent homology module for $\{\widetilde{\mathcal{X}}_n\}$ is equivalent to $(d-k-1)^{th}$ persistent cohomology module of $\{\widetilde{\mathcal{X}}^n\}$. By Equation 1, we have the dimensions of the corresponding homologies are same $\widetilde{H}_k(\widetilde{\mathcal{X}}_n)\simeq\widetilde{H}^{d-k-1}(\widetilde{\mathcal{X}}^n)$. By Equation 2, we have ranks of the maps $\varphi_{ij}:H_k(\widetilde{\mathcal{X}}^i)\to H_k(\widetilde{\mathcal{X}}^j)$ and $\varphi_{ij}^*:H^{d-k-1}(\widetilde{\mathcal{X}}^i)\to H^{d-k-1}(\widetilde{\mathcal{X}}^j)$ are the same. Since the persistence barcode is uniquely determined by these dimensions and the ranks (Lemma 5), we have that the corresponding persistence diagrams are equivalent: $\mathrm{PD}(H_k(\{\widetilde{\mathcal{X}}_n\}))\simeq\mathrm{PD}(H^{d-k-1}(\{\widetilde{\mathcal{X}}^n\}))$. i.e.,

$$\operatorname{PD}_{k}^{\uparrow}(\widetilde{X}, \widetilde{f}) \simeq \operatorname{PD}(H^{d-k-1}(\{\widetilde{X}^{n}\}))$$
 (3)

Now, to finish the proof of Step 1, we need to show equivalence of the persistent cohomology $\operatorname{PD}(H^{d-k-1}(\{\widetilde{\mathcal{X}}^n\}))$ with the persistent homology for superlevel filtration $\operatorname{PD}_{d-k-1}^{\downarrow}(\widetilde{\mathcal{X}},\widetilde{f})$. This step directly follows from the duality of persistent homology and cohomology (Lemma 4) as follows: For superlevel filtration, we use the $\emptyset = \widetilde{\mathcal{X}}^N \subset \widetilde{\mathcal{X}}^{N-1} \subset \cdots \subset \widetilde{\mathcal{X}}^2 \subset \widetilde{\mathcal{X}}^1 \subset \widetilde{\mathcal{X}}^0 = \widetilde{\mathcal{X}}$. Similarly, for persistent cohomology, we use the same filtration in reverse order $\widetilde{\mathcal{X}} = \widetilde{\mathcal{X}}^0 \supset \widetilde{\mathcal{X}}^1 \supset \cdots \supset \widetilde{\mathcal{X}}^{N-1} \supset \widetilde{\mathcal{X}}^N = \emptyset$. Then, by Lemma 4, their barcodes are identical:

$$PD(H^{d-k-1}(\{\widetilde{\mathcal{X}}^n\})) = PD(H_{d-k-1}(\{\widetilde{\mathcal{X}}^n\}))$$
 (4)

Note that to avoid crowded notation, we defined \mathcal{X}^n with $f(\eta) > t_n$ condition, while the original superlevel filtration has \mathcal{X}^n with $f(\eta) \geq t_n$. Hence, in our setup $f(\eta) > t_n$ is equivalent condition to $f(\eta) \geq t_{n+1}$. Therefore, for any k, $\operatorname{PD}(H_k(\{\widetilde{\mathcal{X}}^n\}))$ with our convention shifts each barcode by one $([b,d) \to ([b+1,d+1))$ from the original superlevel $\operatorname{PD}_k^\downarrow(\widetilde{\mathcal{X}},\widetilde{f})$. Hence, we have the equivalence:

$$PD(H_{d-k-1}(\{\widetilde{\mathcal{X}}^n\})) \simeq PD_{d-k-1}^{\downarrow}(\widetilde{\mathcal{X}}, \widetilde{f})$$
 (5)

The proof of Step 1 follows from Equations 3,4,5.

Step 2:
$$\mathrm{PD}_k^{\uparrow}(\widehat{X},\widehat{f}) \simeq \mathrm{PD}_{d-k-1}^{\downarrow}(\widehat{\mathcal{X}},\widehat{f})$$

Proof of Step 2: After Step 1, all we need to do is to relate the homology groups in the persistence modules induced by the extended spheres $\{H_k(\widetilde{\mathcal{X}}_n)\}$ and the extended images $\{H_k(\widehat{\mathcal{X}}_n)\}$.

Recall that $\widetilde{\mathcal{X}}$ is obtained by doubling $\widehat{\mathcal{X}}$. Hence, $\widetilde{\mathcal{X}} - \widehat{\mathcal{X}}$ is an open ball, say U. By applying Mayer-Vietoris sequence to $\widetilde{\mathcal{X}}_n = \widehat{\mathcal{X}}_n \cup \overline{U}$, we see that $H_k(\widetilde{X}_n) = H_k(\widehat{\mathcal{X}}_n)$

for any $0 \le \underline{k} \le d-2$ as $\widehat{\mathcal{X}}_n \cap \overline{U} = \partial \overline{U}$ which is a (d-1)-sphere, and \overline{U} is contractible.

For n < N, $H_{d-1}(\widehat{\mathcal{X}}_n) = H_{d-1}(\widetilde{\mathcal{X}}_n) \oplus \mathbb{Z}$ as removed ball U only effects the homology class corresponding to $\partial \overline{U} = \partial \widehat{\mathcal{X}}_n$ which is nontrivial in $H_{d-1}(\widehat{\mathcal{X}}_n)$ for n < N, while it is trivial in $H_{d-1}(\widetilde{\mathcal{X}}_n)$ for any n. In Alexander duality, this homology class corresponds to the complement of the main connected component, but it is trivial in extended sphere setting. Hence, in the extended image setting, we recover this dual class in $\mathrm{PD}_{d-1}^{\downarrow}(\widehat{\mathcal{X}},\widehat{f})$ as a nontrivial homology class corresponding to the infinite bar removed in reduced persistence diagram $\mathrm{PD}_{0}^{\uparrow}(\widehat{X},\widehat{f})$ in Step 1. In other words, $[t_1,\infty) \in \mathrm{PD}_{d-1}^{\uparrow}(\widehat{\mathcal{X}},\widehat{f})$ which does not exist in extended sphere setting.

Since other dimensions are not affected, and the correspondence in k=0 is recovered as explained in the previous paragraph, the correspondence between the (unreduced) persistence diagrams in the extended image setting follows.

With Step 1 and Step 2, the proof of the theorem follows.

Remark 7 (Explicit Barcode Correspondence) In the theorem above, the explicit barcode correspondence is as follows: Let the sublevel filtration is defined as $\widehat{\mathcal{X}}_1 \subset \cdots \subset \widehat{\mathcal{X}}_{N-1} \subset \widehat{\mathcal{X}}_N = \widehat{\mathcal{X}}$ with $\widehat{\mathcal{X}}_n$ consists of voxels Δ_η with $f(\eta) \leq t_n$. Let the superlevel filtration for the same threshold set is defined as $\widehat{\mathcal{X}}^N \subset \cdots \subset \widehat{\mathcal{X}}^2 \subset \widehat{\mathcal{X}}^1 = \widehat{\mathcal{X}}$ with $\widehat{\mathcal{X}}_n$ consists of voxels Δ_η with $f(\eta) \geq t_n$. Then, if σ represents a k-dimensional topological feature in the sublevel filtration $\{\mathcal{X}_n\}$ with barcode $[b_\sigma, d_\sigma)$, then the last time appears in the sequence at $\widehat{\mathcal{X}}_{d_\sigma-1}$ ($f(\eta) \leq d_\sigma-1$). The complement of $\widehat{\mathcal{X}}_{d_\sigma-1}$ is $(f(\eta) > d_\sigma-1)$ which is equivalent to $\widehat{\mathcal{X}}^{d_\sigma}$ ($f(\eta) \geq d_\sigma$). Hence, the corresponding (dual) (d-k-1)-dimensional topological feature σ^* first time appears in $\widehat{\mathcal{X}}^{d_\sigma}$ in the sequence $\{\widehat{\mathcal{X}}^n\}$, i.e., $b_{\sigma^*} = d_\sigma$. Similarly, one can show $d_{\sigma^*} = b_\sigma$. Therefore, the isomorphism $\varphi: \mathrm{PD}_k^{\uparrow}(\widehat{X},\widehat{f}) \to \mathrm{PD}_{d-k-1}^{\downarrow}(\widehat{\mathcal{X}},\widehat{f})$ can be defined as

$$\varphi: \mathrm{PD}_k^{\uparrow}(\widehat{X}, \widehat{f}) \to \mathrm{PD}_{d-k-1}^{\downarrow}(\widehat{\mathcal{X}}, \widehat{f})$$

where $\varphi([b_{\sigma},d_{\sigma}))=[d_{\sigma},b_{\sigma})=[b_{\sigma^*},d_{\sigma^*})$ Notice that in superlevel filtration since the nested sequence $\{\widehat{\mathcal{X}}^n\}$ comes with decreasing thresholds, with our convention, the birth time $(b_{\sigma^*}=t_i)$ is larger than the death time $(d_{\sigma^*}=t_j)$ in superlevel filtration. Recall that for k=0, the infinite barcode $[t_1,\infty)\in \mathrm{PD}_0^{\uparrow}(\widehat{X},\widehat{f})$ corresponds to $[t_N,t_1)\in \mathrm{PD}_{d-1}^{\downarrow}(\widehat{\mathcal{X}},\widehat{f})$ as explained in Step 2 above.

Remark 8 (Alternative extension for $\widehat{\mathcal{X}}$) *When defining* \widehat{f} *for the extended image* $\widehat{\mathcal{X}}$, *one can use choose the value*

of \widehat{f} on all boundary voxels in $\widehat{\mathcal{X}}-\mathcal{X}$ as $\min f$ instead of $\max f$. The whole proof would go through by swapping sublevel and superlevel filtrations with the function -f instead of f. Note that the original extended image condition $\widehat{f}=\max f$ on $\widehat{\mathcal{X}}-\mathcal{X}$ is automatically satisfied by light background images while alternative extended image condition $\widehat{f}=\min f$ on $\widehat{\mathcal{X}}-\mathcal{X}$ is automatically satisfied by dark background images. This observation is important in applications of our result.